70th International Astronautical Congress (IAC), Washington D.C., United States, 21-25 October 2019.

IAC-19-C1.3.53757

Ejecta orbital and bouncing dynamics around asteroid Ryugu

Alessandro Latino*, Stefania Soldini[a], Camilla Colombo[b], Yuichi Tsuda[c]

* Corresponding author, MSc Space Engineering, Politecnico di Milano, via La Masa 34, 20156 Milano, Italy. *E-mail address:* alessandro.latino@mail.polimi.it

[a] ISAS/JAXA, currently Assistant Professor in Aerospace Engineering, University of Liverpool, Department of Mechanical, Materials & Aerospace Engineering. *E-mail address:* stefania.soldini@liverpool.ac.uk

[b] Associate Professor in Spacecraft Engineering, Politecnico di Milano, Department of Aerospace Science and Technology. *E-mail address:* camilla.colombo@polimi.it

[c] Associate Professor/Hayabusa2 Project Manager, Institute of Space and Astronautical Science (ISAS)/Japan Aerospace Exploration Agency (JAXA). *E-mail:* tsuda.yuichi@jaxa.jp

Abstract

The scientific interest towards asteroids has increased in the last few years, leading to several successful missions such as past Hayabusa (JAXA), Rosetta (ESA), and currently Hayabusa2 (JAXA) and OSIRIS-REx (NASA). Several efforts have been made to study the environmental condition around asteroids, to characterise the dynamical behaviour of orbits about small bodies. One of the most challenging aspects of such missions is to collect and sample asteroids material by means of an on-ground collection, involving landing (or touchdown) and mining. This paper analyses the evolution of the dust dynamics around asteroids in the context of the circular restricted three-body problem, perturbed by the solar radiation pressure and the aspherical potential of the asteroid (J_2 effect). The aim is to carry out an analysis showing if particles ejected by means of a kinetic impactor can be temporary captured around the asteroid, leading to a potential threat for the spacecraft's sampling operations. The main goal of this work is to study the dynamics arising from the re-impact and bouncing of particles ejected from the asteroid surface, analysed by considering non-elastic collisions. These collisions can potentially cause a trail of particles, captured for several months; this mechanism could explain the recent discovery of trails, observed for asteroid *P/2010 A2*. In case these mechanisms are well understood, the asteroid's impact location can be selected, as a function of the high survival on-orbit probability. Since the dynamics involved is different depending on the particles size, as already showed by past works, the solar radiation pressure acceleration acts like a passive in-situ mass spectrometer. Therefore, future missions could consider on-orbit collection as an alternative to landing or touchdown operations. The artificial impact performed during the Hayabusa2 mission makes the asteroid Ryugu the ideal case study.

Keywords: Circular restricted three-body problem; solar radiation pressure; high-order gravity field; dust dynamics around asteroids; collisions and bouncing trajectories; on-orbit collection.

List of symbols

Symbol	Description
C	Jacobi constant
e	Eccentricity
L_i	Non dimensional libration points
$\overline{n}$	Non dimensional mean motion
$\mathbf{r}_{ap}$	Non-dimensional asteroid-to-particle synodic distance vector
$\mathbf{r}_{sp}$	Non-dimensional Sun-to-particle synodic distance vector
$\mathbf{v}_0$	Initial velocity
β	Lightness parameter
γ	Curtain angle
ε_n, ε_t	Normal and tangential coefficients of restitution
θ	Ejection longitude
μ	Adimensional mass parameter

μ_a	Asteroid gravitational mass parameter
μ_s	Sun gravitational mass parameter
ϕ	Solar phase angle
Ω	Right ascension of the ascending node
ω	Argument of pericentre

List of acronyms

Acronym	Description
2BP	Two-Body Problem
AU	Astronomical Unit
CR3BP	Circular Restricted Three-Body Problem
JAXA	Japan Aerospace Exploration Agency
NASA	National Aeronautics and Space Administration
NEO	Near-Earth Objects
SCI	Small Carry-on Impactor
SRP	Solar Radiation Pressure
TOF	Time Of Flight
ZVC	Zero Velocity Curves

1. Introduction

Most of NEO observed so far have a fine layer of regolith material deposited on the asteroid surface, most likely as a result of micro-meteoroid bombardment [1]. Therefore, it is likely to produce ejecta by means of a small kinetic impactor and then study the orbital evolution of the particles. A long survival of these particles into asteroid's orbit could pose a potential threat to spacecraft operations, since they could degrade or damage instrumentation and reduce visibility and communications. In April 2019 Hayabusa2 mission succeeded in creating an artificial crater on the surface of asteroid Ryugu by means of the SCI on board the spacecraft. In the ideal scenario of the 2BP, an ejected particle with a velocity below the escape one will re-impact the asteroid surface. In reality, due to perturbations (non-uniform gravitational field, solar radiation pressure, non-elastic collisions, …) the ejecta could potentially remain in orbit around the small body for several months. Indeed, Pinto et al. [2] used the augmented Hill problem to study the temporary orbital capture of ejecta. The aim of their work was to identify the ejecta launch site locations that could lead to the largest number of ejecta particles being naturally captured into families of periodic orbits, by making use of the invariant manifold theory.

In the last few years, several efforts have been made to study and understand the behaviour of particles orbiting around small bodies. Krivov et al. [3] studied the dynamics of impact ejecta from Phobos and Deimos, the moons of Mars, for μm sized particles, using the Lagrangian non-singular elements equations of motion. Hamilton and Krivov [4] rewrote the orbit-averaged equations of motion (including SRP, tidal force of the Sun, planetary oblateness and electromagnetism) as a semicanonical system. They derived the integral of motion, used to investigate the evolution of the phase space; the same technique was then applied by Colombo et al. [5] to find a new set of quasi-frozen heliotropic orbits around the Earth. The work of Russell et al. [6] showed the utility of heliotropic orbits, which allow low-inclined and long-lifetime orbits by exploiting the combined effects of SRP and irregular gravity of the asteroid.

This paper investigates the dynamics of particles ejected from the asteroid surface after a kinetic impact, in an environment perturbed by the Sun gravitational pull, the solar radiation pressure and the aspherical potential of the asteroid. The orbital dynamics is coupled with the asteroid's surface bouncing mechanism, which produces new trajectories and rises the complexity of the overall orbital capture mechanism. The dynamics arising from the re-impact and bouncing of particles ejected from the asteroid surface is analysed by considering non-elastic collisions. By understanding this mechanism, the asteroid's impact location could be selected, as a function of the high survival on-orbit probability. Since the dynamics involved is different depending on the particles size, as already showed by Garcia et al. [7], the solar radiation pressure acts like a passive in-situ mass spectrometer. Therefore, future missions could consider on-orbit collection as an alternative to landing or touchdown operations.

The paper is organized as follows: Section 2 focuses on the the CR3BP equations of motion perturbed by SRP and J_2, together with the concept of zero velocity curves. In Section 3, the coupled bouncing-orbital dynamics model is proposed, while Section 4 is dedicated to present the parameters and initial conditions setting. Section 5 and 6 are devoted to the results and concusions, respectively.

2. The Photo-gravitational circular restricted three-body problem

In this section, the CR3BP perturbed by the solar radiation pressure and the non-uniform gravitational field of the asteroid is defined.

2.1 Solar radiation pressure effect

For a non-Sun pointing or non-spherical object, SRP is a non-conservative force. In the model proposed, dust particles are approximated as spherical object, therefore the the SRP effect is conservative. Following loosely McInnes [8], the magnitude of the SRP a_{SRP} can be written as

$$a_{SRP} = P_{SRP} \frac{A_{Sun}}{m} c_R \tag{1}$$

where A_{Sun} is the projected area exposed to the Sun, m is the particle mass and c_R the reflectivity coefficient. This last term is in general a vector quantity, and its modulus can vary from 0 to 2, where 0 indicates a translucent particle (no SRP), 1 a black body (all radiation is absorbed) and 2 a completely reflective surface.

The lightness parameter β will be used, which is the ratio between the SRP acceleration and the solar gravitational acceleration. Furthermore, the acceleration vector associated to SRP can be written as

$$\mathbf{a}_{SRP} = \beta \frac{\mu_{Sun}}{r_{sp}^2} \hat{\mathbf{r}} \tag{2}$$

where $\hat{\mathbf{r}}$ is the particle-to-Sun direction. The above expression is valid for a Sun-pointing surface; indeed, the main advantage of the cannonball model is that the SRP acceleration can be written as the potential of the SRP forces, as follows:

$$\mathbf{a}_{SRP} = \bar{\nabla} V_{SRP} \hat{\mathbf{r}} \text{ , with } V_{SRP} = -\beta \frac{\mu_{Sun}}{r_{sp}} \tag{3}$$

2.2 Equations of motion

The non dimensional photo-gravitational CR3BP equations of motion expressed in a synodic reference frame (Fig. 1) are:

$$\begin{cases} \ddot{x} - 2\bar{n}\dot{y} = V_{/x} \\ y + 2\bar{n}\dot{x} = V_{/y} \\ \ddot{z} = V_{/z} \end{cases} \tag{4}$$

where x, y, z and $\dot{x}$, $\dot{y}$ are the non-dimensional particle positions and velocities in the rotating frame, while $\bar{n}$ is the adimensional mean motion, equal to unity in this case. The total potential V is

$$V = \frac{1}{2}\left(x^2 + y^2\right) + \frac{\left(1-\beta\right)\left(1-\mu\right)}{r_{sp}} + \frac{\mu}{r_{ap}} \tag{5}$$

where the adimensional Sun-to-particle and asteroid-to-particle distances (r_{sp}, r_{ap}) are

$$\begin{cases} r_{sp} = \sqrt{\left(x+\mu\right)^2 + y^2 + z^2} \\ r_{ap} = \sqrt{\left(x+\mu-1\right)^2 + y^2 + z^2} \end{cases} \tag{6}$$

The normalisation parameters which make the above equations adimensional are listed in Table 1.

Table 1: Normalisation parameters for the Sun-Ryugu system

Length unit, l [km]	1.19 AU
Mass unit, M [kg]	$\approx 1.989 \cdot 10^{30}$
Time unit, τ [s]	$6.516592779 \cdot 10^{6}$
Velocity unit, v [km/s]	27.32

2.3 Libration points

Also called Lagrange points, these equilibrium points are the location in space where the orbiting particle would appear permanently at rest with respect to the primaries, while for an inertial observer it would move in circular orbit around the Sun and the asteroid. The libration points can be found by equating the left hand side of Eq. (4) to zero. In the CR3BP, five equilibrium points exist: three collinear points (L_1, L_2 and L_3), located along the Sun-asteroid line ($y = z = 0$), and two equilateral points, symmetric with respect to the x-axis ($y \neq 0$, $z = 0$).

Since the libration points are equilibrium locations in which the accelerations cancel out, when SRP is taken into account, an additional perturbing term arises, which modifies the equilibrium points position from the original one in the CR3BP. In this case, they are called “artificial” or “pseudo” libration points: they shift towards the bigger primary (Sun),

as schematized in Fig. 1 in which only the collinear equilibrium points are sketched.

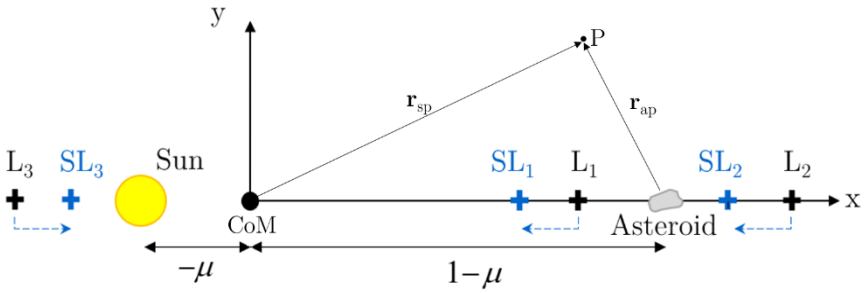

Fig. 1: Relative non-dimensional positions of the Sun, asteroid and particle (P) in a synodic reference frame. The collinear libration points (+) shift into the pseudo libration points (+) when SRP is involved.

2.4 Zero velocity curves

Despite Eq. (4) has no close form analytical solution, for a conservative system it has a well known integral of motion, the so-called Jacobi constant C:

$$C = x^2 + y^2 + \frac{2(1-\mu)(1-\beta)}{r_{sp}} + \frac{2\mu}{r_{ap}} - v^2 \qquad (7)$$

where v is the speed of the orbiting particle. This quantity is conserved through the motion of the particle, meaning that if an energy level and an initial position are fixed, then the magnitude of the velocity at any point is uniquely determined as well. On the other hand, if the velocity is prescribed to be zero at a given energy, this will determine a set of initial conditions which implicitly solve the equation

$$x^2 + y^2 + \frac{2(1-\mu)(1-\beta)}{r_{sp}} + \frac{2\mu}{r_{ap}} - C = 0 \qquad (8)$$

The solution set of this equation will be a two dimensional surface (not necessarily compact or connected [9]) in the configuration space, which tells a lot about the possible dynamics a particle can have, at a given energy level. Indeed, a particle reaching the zero velocity curves arrives, as the name suggests, with no velocity, so that it cannot go through or past it because it would require that $v^2 < 0$, which is clearly unphysical.

By computing the Jacobi integral in correspondence of the libration point L_2, setting the velocity to zero, the Jacobi constant C_2 can be found. An energy level $C \geq C_2$ ensures a bounded motion around the asteroid, since the zero velocity curves are closed, meaning that particles will eventually re-impact the asteroid surface, sooner or later. An energy level $C = C_2$ is the maximum allowed to avoid particles to escape through L_2, and it also offers the biggest possible region for bounded natural motion. Furthermore, if this threshold is decreased, a bottleneck opens at the libration point, allowing ejecta to escape (Fig. 2). This energetic approach will be used in the paper to exploit different possible natural dynamics of ejected particles.

2.5 Effect of J2 on the CR3BP

Gravitational potential modelling is a crucial aspect to tackle when dealing with irregular shaped bodies, such as asteroids. Typically, there are very few information about the asteroid mass, shape and density, making an "a priori" gravitational model difficult to develop. As a matter of facts, most of the high precision data about the asteroids physical characteristics have been collected by spacecrafts flybys, or through close observations.

Spherical harmonics model is the standard tool to use when dealing with high-order gravitational fields, typically used when the body differs slightly from the spherical shape (*i.e.* planets, moons). To take into account the oblateness of the smaller primary into the CR3BP equations of motion, first the mean motion of the primaries (*i.e.* Sun and the asteroid) around their common barycentre must be redefined [10]. The mean motion of the primaries is assumed circular, lying on the $z = 0$ plane. Its adimensional expression is

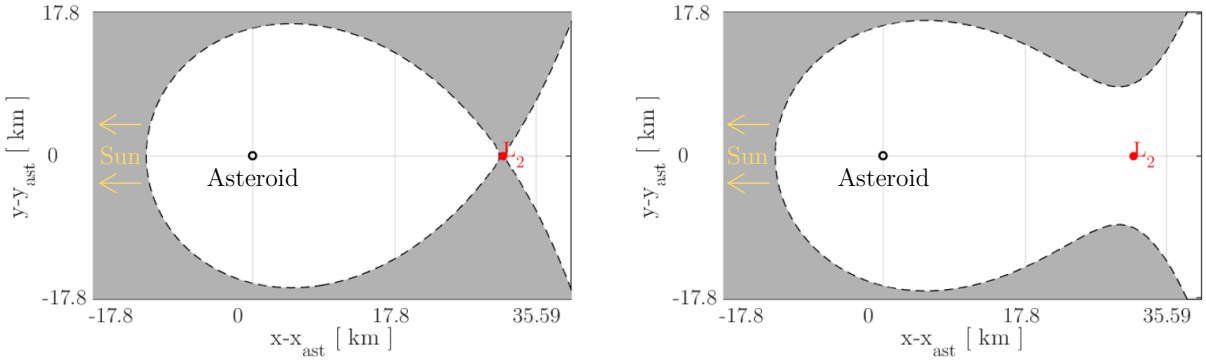

Fig. 2: Zero velocity curves for an energy level $C = C_2$ (left) and $C < C_2$ (right)

$$\bar{n}^2 = 1 + \frac{3}{2} J_2 \left(\frac{r}{R_0} \right)^2 = 1 + \frac{3}{2} J_2 \bar{r}^2 \tag{9}$$

where r is the mean radius of the asteroid, R_0 is the Sun-to-asteroid mean distance and J_2 is the first gravity field coefficient of the harmonic expansion.

If a triaxial ellipsoid is considered, with dimensions $a \geq b \geq c$, it is possible to compute recursively all the $J_{2l,2m}$ gravity field coefficients, with $l \geq 1$, $m \geq 0$ [11]. The coefficients up to $J_{4,4}$ can be written in a simple closed form, as follows:

$$\begin{cases} J_2 = \dfrac{1}{5r^2}\left(\dfrac{a^2+b^2}{2} - c^2 \right) = 0.008347066115702 \\ J_{2,2} = \dfrac{1}{20r^2}\left(b^2 - a^2 \right) = -0.001556342975207 \\ J_4 = -\dfrac{15}{7}\left(J_2^2 + 2J_{2,2}^2 \right) = -0.000159681256398 \\ J_{4,2} = -\dfrac{5}{7} J_2 J_{2,2} = 0.000009279212651 \\ J_{4,4} = -\dfrac{5}{28} J_{2,2}^2 = -0.00000043253633 \end{cases} \tag{10}$$

where the values used to compute them are the ones associated to Ryugu ($r = 440$ m, $a = 446.5$ m, $b = 439.7$ m, $c = 433.9$ m) [12].

It is possible to add the 3rd body (*i.e.* the orbiting particle) without changing the expression of the mean motion since, by definition, the third body is massless, and it does not affect the motion of the primaries. However, the particle motion will be affected by the oblateness of the asteroid, which will appear in the adimensional potential expression of Eq. (5), leading to the following expression

$$V = \frac{1}{2}\bar{n}^2\left(x^2 + y^2\right) + \frac{\left(1-\mu\right)\left(1-\beta\right)}{r_{sp}} + \\ + \frac{\mu}{r_{ap}}\left[1 - \frac{1}{2} J_2 \left(\frac{\bar{r}}{r_{ap}} \right)^2 \left(3\frac{z^2}{r_{ap}^2} - 1 \right) \right] \tag{11}$$

By using Eqs. (10) and (9) into Eq. (4), it is possible to find the adimensional equations of motion for the CR3BP perturbed by SRP and J_2.

When adding the effect of the smaller primary oblateness, since the equations of motion change, the position of libration points is affected as well. To find the location of the collinear libration points, three different 7th order polynomials must be solved numerically. As visible in Fig. 3, the behaviour of the equilibrium points is quite different: for L_1, since increasing values of β bring the libration point closer to the system barycentre, the effect of the smaller primary oblateness becomes negligible, hence the difference between the SRP-only and SRP+J_2 libration points is zero. For L_2, since when $\beta \to 1$ the equilibrium point moves closer to the asteroid, the J_2 disturbance becomes more and more relevant.

However, it should be noted that, due to the smallness of the asteroid, the shift is of the order of centimetres, which, in practice, is negligible.

3.Impact model

To link the orbital dynamics with the physical model behind the bouncing behaviour, an impact map should be implemented. This method requires the knowledge of the coefficient of restitution e, which is usually a single scalar quantity, defined as the ratio of the final to initial relative velocity between two objects after they collide. It varies from 0 to 1,

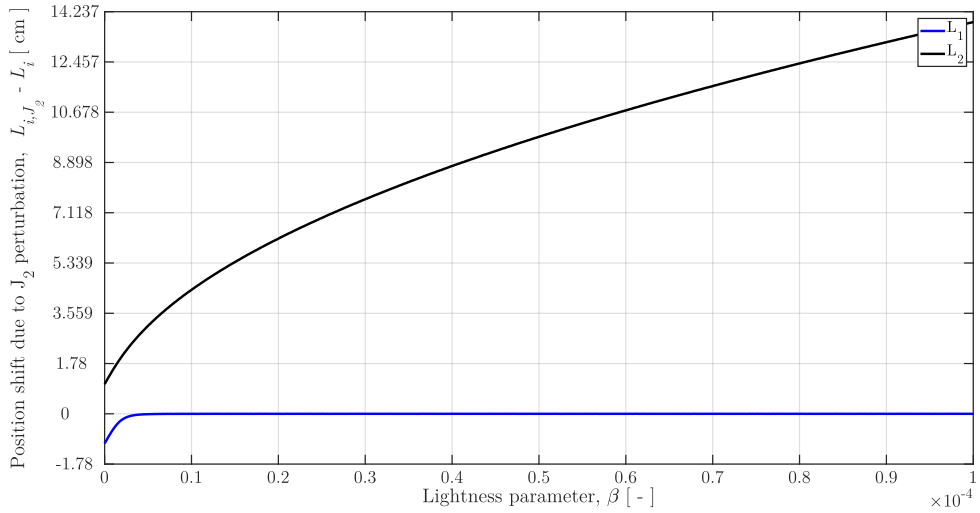

Fig. 3: Position shift for SRP+J_2 libration point with respect to SRP-only disturbance. Both L_1 (blue) and L_2 are displayed

where 0 refers to a perfectly inelastic collision, while 1 is associated to a perfectly elastic one[1]. In the case in exam, the particle impacts on an immovable surface (*e.g.* the asteroid), so that the coefficient of restitution expression simplifies to

$$e = \frac{v_f}{v_i} \tag{12}$$

where v_f and v_i are the speed after and before the impact event, respectively. When the collision happens at an oblique angle, or when rotation is involved, the coefficient of restitution is split up in normal (ε_n) and tangential (ε_t) components, which are applied to their respective velocity components (*e.g.* v_n and v_t). During the impact, the kinetic energy is lost to rotational energy, plastic deformation and heat. Depending on the chosen values, the velocity after the impact will change accordingly: as visible in Fig. 4a, a dissipative reflective bouncing is achieved when $\varepsilon_n = \varepsilon_t$. To allow also the direction of the velocity after the impact to change, the two coefficients of restitution must be different between each other (Fig. 4b).

To implement the impact map, first the angle α between the x-axis and the local tangent to the surface must be computed, to rotate the velocity in the local $\{t,n\}$ reference frame through the rotation matrix $\mathbf{R}$ (Fig. 5a)

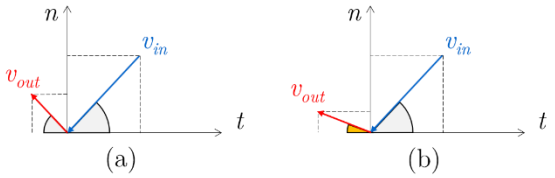

Fig. 4: Velocity after impact for (a) dissipative reflective bouncing ($\varepsilon_n = \varepsilon_t$) and (b) dissipative diffusive bouncing ($\varepsilon_n \neq \varepsilon_t$)

$$\mathbf{R} = \begin{bmatrix} \cos\alpha & \sin\alpha & 0 \\ -\sin\alpha & \cos\alpha & 0 \\ 0 & 0 & 1 \end{bmatrix} \tag{13}$$

Then, to solve the impact and obtain the output velocity vector $\mathbf{v}_{tn}$, expressed in the normal and tangential reference frame, the matrix $\mathbf{E}$ containing the restitution coefficients is applied (Fig. 5b)

$$\mathbf{E} = \begin{bmatrix} \varepsilon_t & 0 & 0 \\ 0 & -\varepsilon_n & 0 \\ 0 & 0 & -1 \end{bmatrix} \Rightarrow \mathbf{v}_{tn} = \mathbf{E}\mathbf{R}\mathbf{v}_{in} \tag{14}$$

Finally, the output velocity must be rotated back to the cartesian reference frame, to use it as a new initial condition for the orbit propagator (Fig. 5c)

$$\mathbf{v}_{out} = \mathbf{R}^T \mathbf{v}_{tn} \tag{15}$$

The impact angle γ_{in} relative to the local reference

[1] The coefficient of restitution can assume a value greater than 1 if there is energy gain during the collision from an internal energy decrease (*e.g.* chemical reaction) that contributes to the post-collision velocity

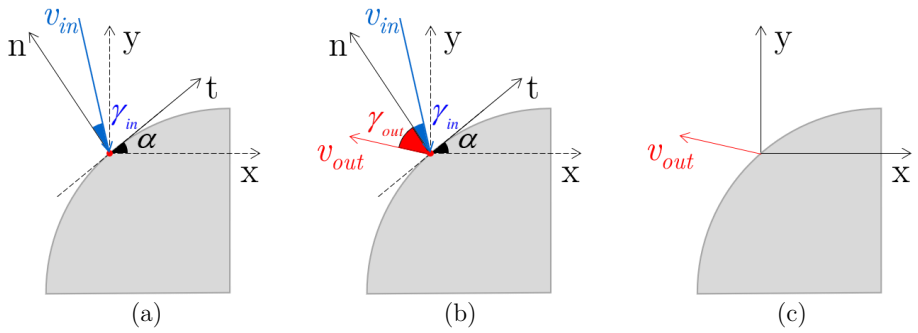

Fig. 5: Impact map step-by-step in the xy plane. The z-axis points outward

frame depends on the incoming velocity v_{in} of the particle trajectory prior the impact event, while the modulus and direction (γ_{out}) of the output velocity v_{out} is related to the selected coefficients of restitution. Collisions are assumed to happen instantaneously, so that the position does not change during the impact event.

During the process described above, it is essential to fix a threshold which discriminates between rebounding and landing (rolling) dynamics. Yang [13] suggests to estimate the height of bouncing off and compare it with a numeric tolerance. This can be achieved by imposing that the vertical component of the equivalent parabolic trajectory the particle would follow is zero, which allows to compute the maximum heght l as

$$l = \frac{v_n^2}{2g_0} \tag{16}$$

where g_0 is the normal component of the local gravitational acceleration at the impact point, while v_n is the normal component of the velocity after the impact occurred. Comparing this value to an arbitrary tolerance l_ε, two cases can be identified:

- *Bouncing* ($l > l_\varepsilon$), for which the particle is still orbiting, after the collision. In this scenario, the new initial condition is used by the orbital propagator to find the subsequent trajectory.
- *Landing* ($l < l_\varepsilon$), in which the particle starts rolling on the surface. In this case, the simulation stops.

The tolerance l_ε should be reasonably low (*e.g.* 10 *cm*) to properly differentiate between rolling and bouncing dynamical behaviour. However, this constraint can be considerably relaxed from tens up to hundreds of meters from the asteroid surface. Indeed, as explained in the next section, the energy associated to this condition is such that the ZVC shrink around the asteroid, leaving a very small allowed region for natural motion. This consideration helps also to reduce the number of bouncing obtained numerically, which are typically less than in real life applications [14]. Furthermore, it mitigates the uncertainties arising from the lack of knowledge of the surface features of asteroid Ryugu, which are strictly related to the coefficients of restitution used.

4.Parameters setting and initial conditions

As explained in Section 2.4, the energy of the system is allowed to span between two values, which in turns ensure the ejecta to have a bounded natural motion or to escape through the bottleneck at L_2. The other crucial parameter to set is the lightness parameter, which can be made explicity dependant on the the particle density ρ_p and the particles radius r_p

$$\beta = P_{SRP-1AU} \frac{r_{es}^2}{\mu_{Sun}} \frac{3}{2\rho_p r_p} c_R \tag{17}$$

The reflectivity coefficient is set to $c_R = 2$, corresponding to an ideal specular reflection, while the particles density is chosen to be $\rho_p = 3.2$ g/cm^3.

The only parameter left is the particles radius, which should be allowed to range between a minimum and maximum value. Virtually there is no upper limit imposed by the problem itself, so it was set to be $r_p = 10$ cm (Fig. 6a). The minimum value is instead constrained: the location of libration points directly depends on the lightness parameter β and, therefore, on the particle radius r_p. For increasing

values of β (*i.e.* decreasing particle radius) L_2 shifts towards the asteroid surface and moves inside of it. In particular, when the particle radius is 19 μm, the Lagrangian point L_2 is located on the surface of Ryugu. When this happens, the allowed regions are partially inside the asteroid, clearly impossible to exploit, and partially located on the dark side of the asteroid (Fig. 6b). A particle radius of $r_p = 1$ mm implies that L_2 is located at 3 km from the asteroid surface. This in turn set the maximum value of the lightness parameter ($\beta_{max} \approx 7.08 \cdot 10^{-4}$), for which the zero velocity curves ensure a suitable allowed region for particles natural motion (Fig. 6c). Since the Jacobi constant is a quantity conserved through the motion of the particle, if an energy level and an initial position are fixed, then the magnitude of the velocity at any point is uniquely determined as well. This characteristic can be exploited to carry out an energetic approach: for example, if the energy level is C_2, the correspondent ejection velocity is

$$v_{ej}(x, y, \beta) = \sqrt{C(x, y, \beta) - C_2} \tag{18}$$

where C is given by Eq. (7). The dependence on both longitude (here represented by the x-y couple) and lightness parameter is made explicit: indeed, different sized particles ejected from different longitudes θ will have different ejection velocities, at a fixed energy level (Fig. 7).

By fixing the particle size r_p, the ejection velocity corresponding to the energy level set will change with the ejection site. Instead, if the ejection

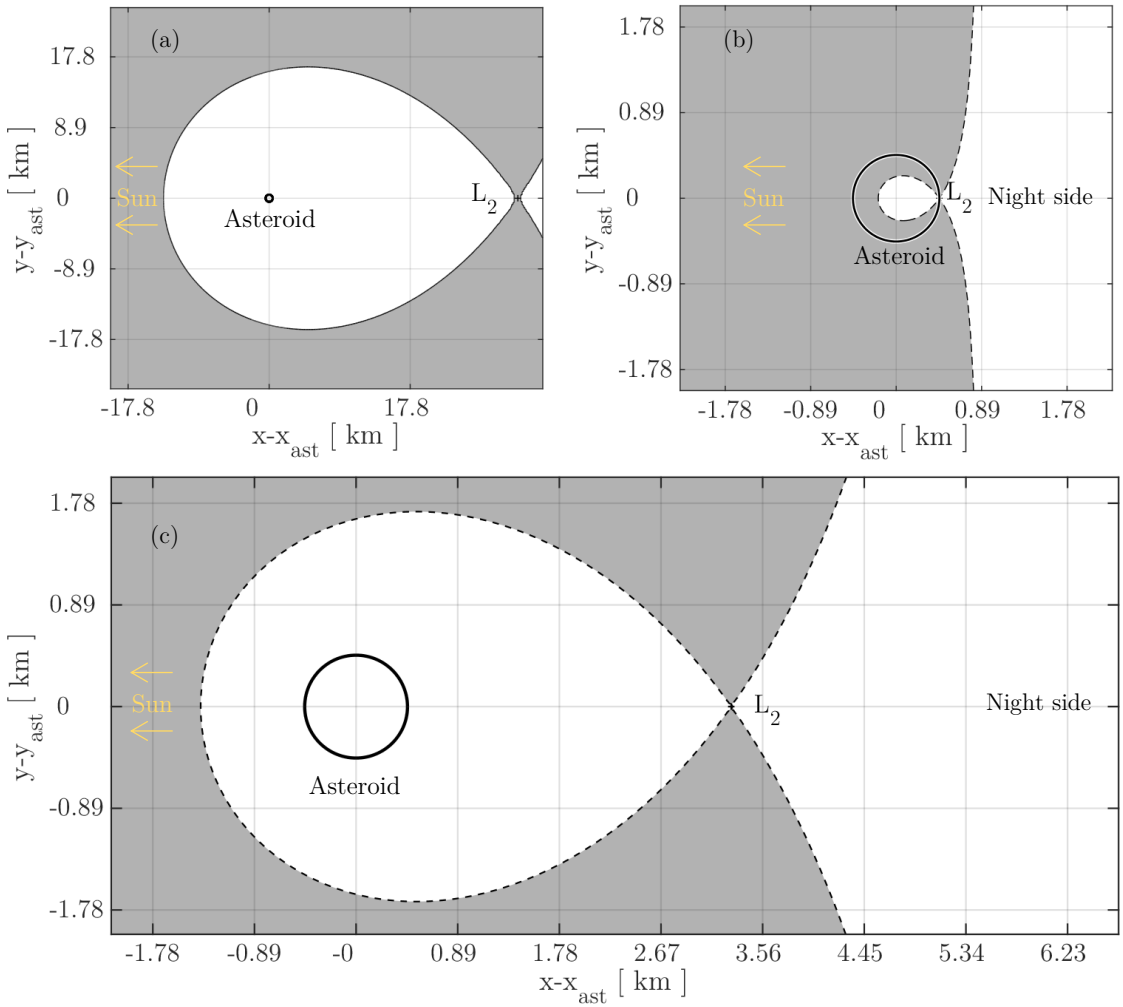

Fig. 6: Zero Velocity curves corresponding to $r_p = 10$ cm (a), $r_p = 19$ μm (b) and $r_p = 1$ mm (c)

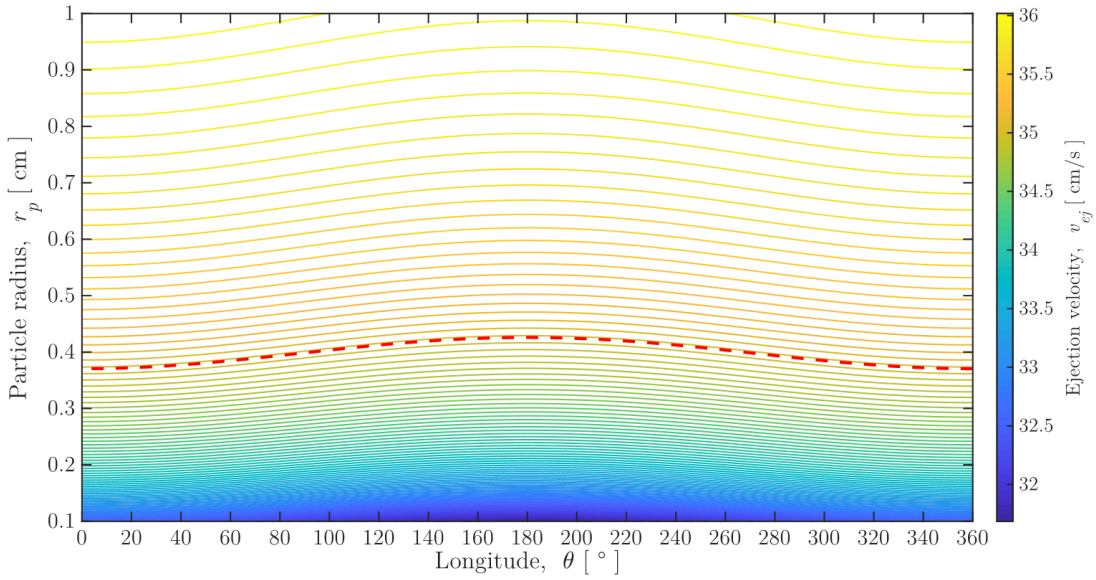

Fig. 7: Ejection speed as function of the longitude and particle radius (1 mm to 1 cm), for a fixed energy level $C = C_2$

velocity is chosen (red dashed line), two regions are identified: one for which ZVC are surely closed (above the red line) and another for which a bottleneck opens at L_2. This means that, at a fixed ejection velocity, bigger particles will surely re-impact the asteroid surface, while smaller ones can potentially escape. Once the ejection speed is set, the direction of ejection should be defined as well, in order to form a set of feasible initial conditions to start the integration of the dynamical problem. Asteroids are typically in a stable rotation about their maximum moment of inertia, which offers the minimum energy for the rotational state. This means that the initial velocity should take into account the rotative contribution of the small body, which gives an extra push to the particle. This effect is usually considered in high fidelity models, whose equations of motion are expressed in a body fixed reference frame.

This is however outside the scope of the paper, which aims to carry out an analysis based on a simplified model, to give a qualitative picture of the dynamics involved. Furthermore, being aware of this problem allows to exclude, for example, the possibility of having a purely radial initial velocity (Fig. 8a) and to consider instead the ejection velocity inclined by an arbitrary angle γ (Fig. 8b). The direction γ varies between $\pm 90°$, so that the initial velocity vector $\mathbf{v}_0$ is given by

$$\mathbf{v}_0 = v_{ej} \cos\left(\gamma + \theta\right)\mathbf{i} + v_{ej} \sin\left(\gamma + \theta\right)\mathbf{j} \qquad (19)$$

where v_{ej} is the ejection speed associated to the energy level fixed.

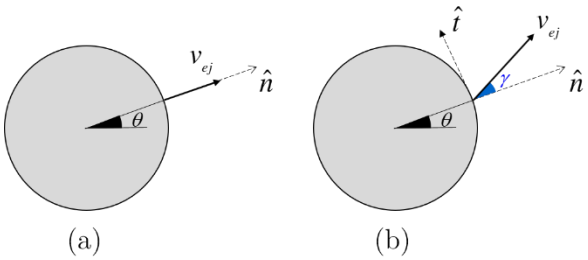

Fig. 8: Initial ejection velocity: (a) purely radial and (b) inclined

5. Application to Hayabusa2's SCI impact experiment

5.1 First impact global behaviour

To get a qualitative picture of the particles dynamics around Ryugu, the first impact location for different ejection longitudes θ was analysed, as function of the curtain angle of ejection γ (Fig. 9). The columns refer to different energy level, $C = C_2$ for the first and $C = C_{min}$ for the second one, while the rows are associated with increasing values of particle radius, $r_p = 1$ mm, $r_p = 1$ cm and $r_p = 10$ cm, respectively.

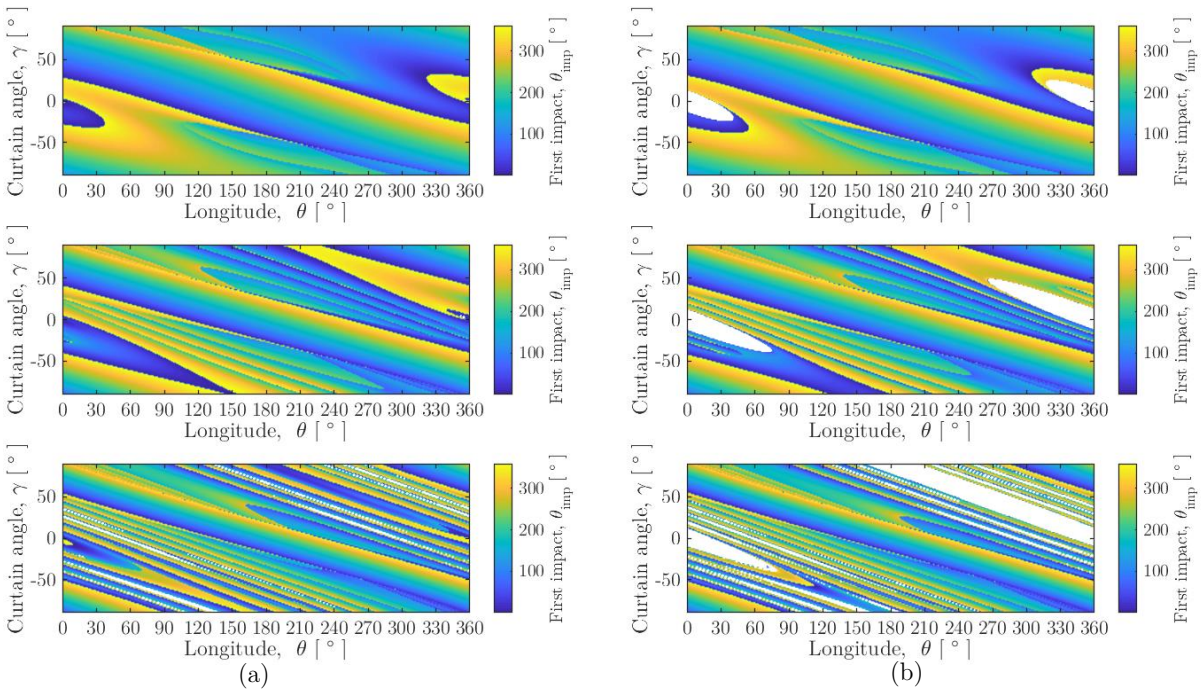

Fig. 9: Number of pericentre passages as function of the ejection longitude θ and the curtain angle γ. Column (a) is associated to $C = C_2$ and column (b) to $C = C_{max}$, while the rows refer to different particle size, $r_p = 1$ mm, $r_p = 1$ cm and $r_p = 10$ cm

When the energy level is the one of L_2, the resulting possible natural motion is bounded around the asteroid, meaning that all particles will re-impact the asteroid surface, sooner or later. Therefore, the white regions appearing in Fig. 9a (second and third rows) are associated to particles which did not collide with the asteroid within the integration time, set to 3 months. These "no-impact" regions apper clearly when $r_p = 10$ cm: smaller particles perform less revolution around the asteroid, colliding the surface at a certain point, often shortly after their ejection. When the energy level is decreased down to C_{min}, which is associated to the maximum ejection velocity from the asteroid surface, the "no impact" regions start appearing also for 1 mm particles (Fig. 9b). As confirmed by Fig. 10, the behaviour is due to particles which directly escape from the bottleneck at L_2, which is open for this energy level. In particular, Fig. 10a shows how the ejection sites and the number of particles escaping through the bottleneck increases evidently when passing from 1 mm to 1 cm size. Furthermore, when the particle radius is increased to 10 cm (Fig. 10b), both escaping and bounded trajectories can be appreciated. This is because the SRP influence is lower with respect to smaller particles, which are easily "blown away" through the bottleneck.

5.2 Energy dissipation

Since particles freely move with their natural motion around the asteroid, the energy is only dissipated through the collision mechanisms with the surface. Estimating how much energy will be dumped on the first impact (and on the successive ones) is a difficult question, because this is highly dependent on the relative angle between the incoming velocity and the surface. Due to the irregular topology of Ryugu (as well as of any asteroid), which presents hills, valleys and rocks of various sizes, it is of high complexity to represent all the impact angles a particle could encounter. However, the physical meaning of this simplified model still holds [15]: high impact angles (*i.e.* velocity almost tangent to the surface) will cause either a high friction if the particle cannot rotate or, more likely, a rolling motion. This latter scenario is the most suited in the context of spherical grains model: as the rolling takes place, part of the kinetic energy is converted into angular energy.

The energy dissipation mechanism can be easily appreciated by investigating some test cases:

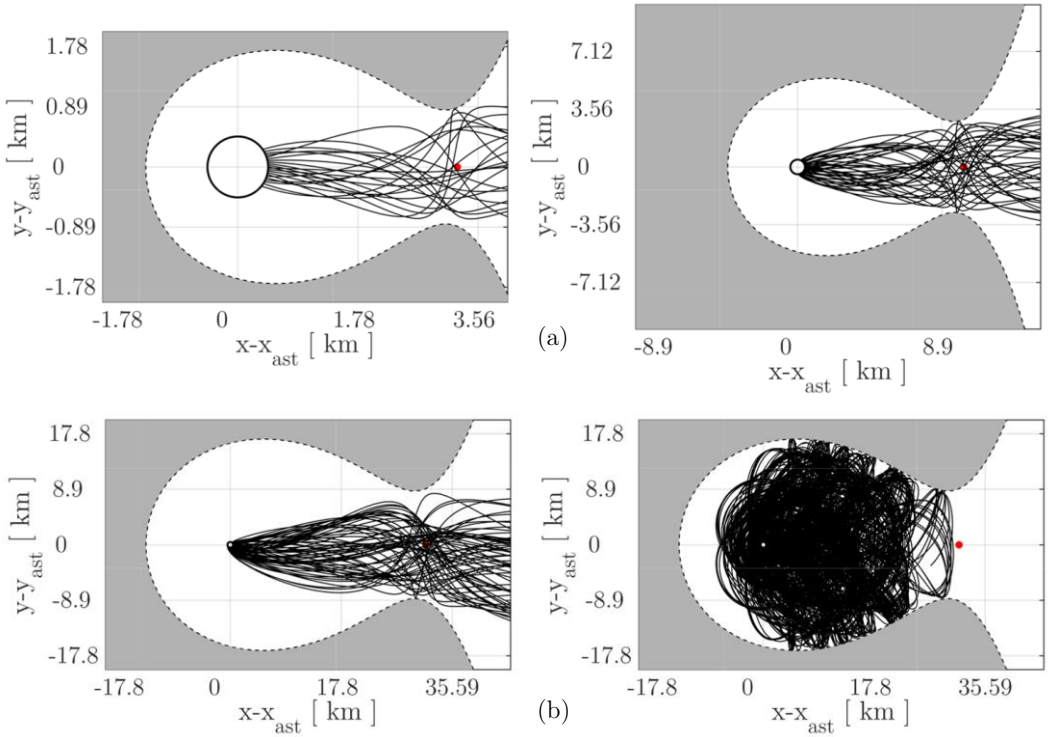

Fig. 10: No-impacts trajectories for (a) $r_p = 1$ mm (left) and $r_p = 1$ cm (right) and (b) $r_p = 10$ cm, divided into escape trajectories (left) and high-survival orbits bounded around the asteroid (right). The red dot refers to the position of L_2.

Fig. 12 refers to an ejection site $\theta = 139°$, with an ejection angle of –85.5°. The energy is the minimum one (bottleneck opened at L_2) while the coefficients of restitution are fixed to $\varepsilon_n = 0.6$ and $\varepsilon_t = 0.714$. The continuous black line represents the energy (scaled by the initial energy) associated to the particle trajectory; as expected, the energy remains constant up to when an impact event occurs (red dot). The dotted blue line refers to the energy associated to the trajectory if it had zero velocity (*i.e.* it is the potential associated to the trajectory).

Recalling that the total energy of the system is

$$E = -\frac{C}{2} = \frac{1}{2}\left(\dot{x}^2 + \dot{y}^2 + \dot{z}^2\right) - V \qquad (20)$$

where the total potential V is given by Eq. (11), it follows that the dissipation decreases the kinetic part of the above equation. Indeed, the total potential depends only on the position of the particle: since both ejections and impacts happen on the asteroid surface, where the potential is more or less the same regardless the longitude, V does not change significantly from the ejection to the impact event. When the blue and the black lines are closer, the trajectory is "touching" the ZVC, while the peaks correspond to the trajectory pericentres, where the velocity is maximum. After the first impact, the new trajectory has a much smaller allowed region to move into (Fig. 11), so that the successive bouncing happen before the particle is able to perform one revolution around the asteroid, as indicated by the dotted blue line. The trajectories after the first bounce are strictly related to the selected coefficients of restitution, as well as on the impact point and angle of impact.

As reported by Van Wal [14], the laser rangefinder onboard the Hayabusa estimated a normal coefficient of restitution $\varepsilon_n \approx 0.84$ for Itokawa. Although the author pointed out also that, due to a 3 min measurement gap, the accuracy of this value can be questionable, it is reasonable to expect also "off-nominal" conditions for Ryugu's coefficients of restitution, due for example to the diverse topology of the asteroid. For this reason, to answer the question of what could happen if the coefficients of restitution for Ryugu have been underestimated, it can be

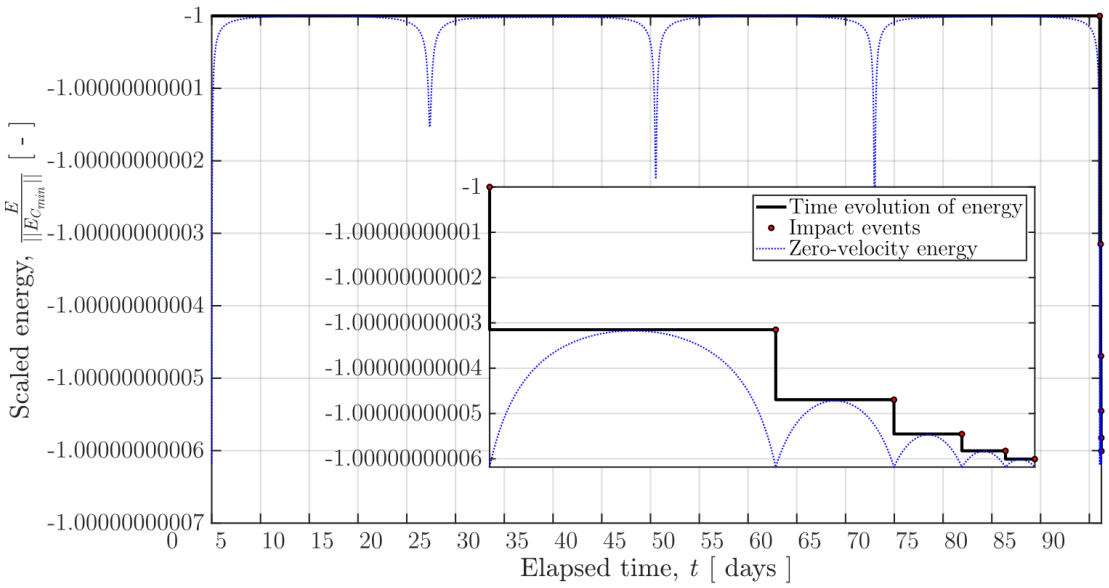

Fig. 12: Time history of the energy dissipation for a particle ejected from $\theta = 139°$ latitude with an ejection angle $\gamma = -84.5$

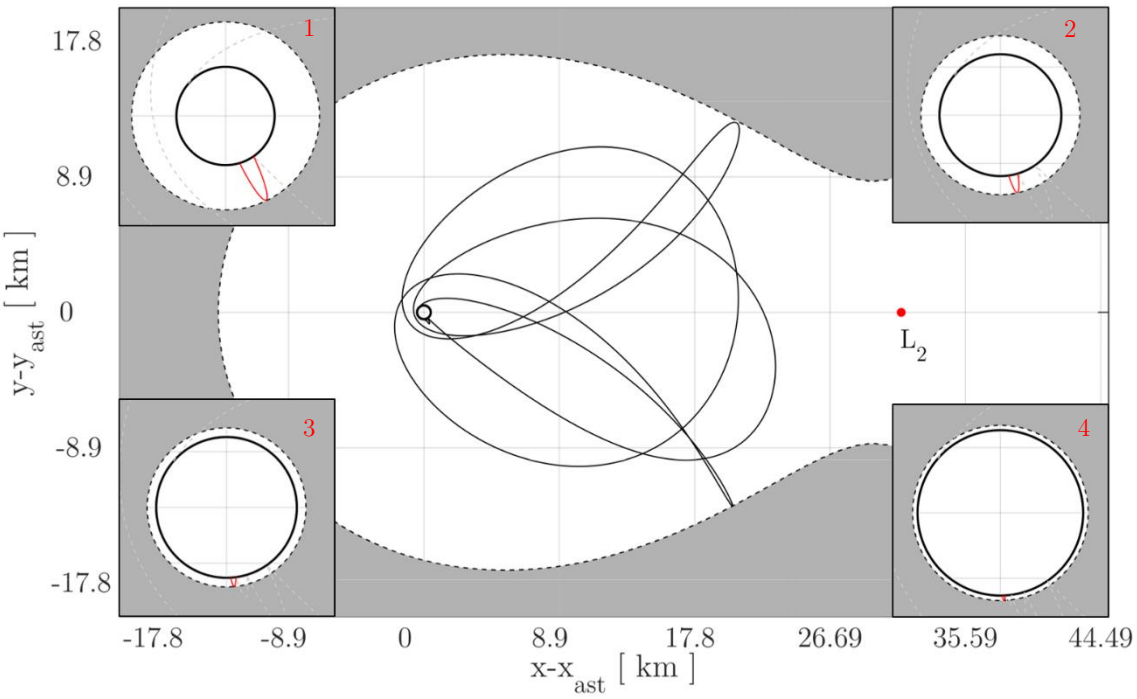

Fig. 11: Associated trajectory bounded by the ZVC (grey regions). The successive bouncing are shown in the boxes: the first impact (top left), second (top right), third (bottom left) and last (bottom right). The allowed region shrinks after each bounce

interesting to investigate also off nominal cases.

When the coefficients of restitution are increased, the more elastic surface guarantees multiple revolutions, even after the first and successive bouncing. From the energy plot (Fig. 13), it can be distinguished the initial ejection phase, characterized by few revolutions around the asteroid, followed by a multi-revolution transient, right after the first impact. Even after the second and third impacts, the particle perform more than one revolution, up to when it starts

a multiple impacts phase, which completely dissipates the energy.

With this approach, it is then possible to detect the time intervals in which impacts happen more frequently, as well as deduce if a "no-impact" time span is due to big orbits (few revolutions) or multiple revolution orbits, which are potentially a threat for the spacecraft operations. On the other hand, these information can represent the starting point to plan an on-orbit collection campaign, scheduled for those time windows in which the trajectories are more crowded in particles.

a planar case, using orbit-averaged Lagrange's planetary equation over one revolution. This method was also used by Colombo et al. [5] to design a new set of quasi-frozen heliotropic orbits at non-zero inclination for a swarm of small spacecrafts for Earth observations. Those papers will be used as references in this thesis to develop the semi-analytical model.

To write the orbit-averaged equation of motion as a semi-canonical system, a change of variables is needed:

$$\phi = \Omega + \tan^{-1}\left(\frac{\cos i \sin\omega}{\cos\omega}\right) - \lambda_s + \pi \qquad (21)$$

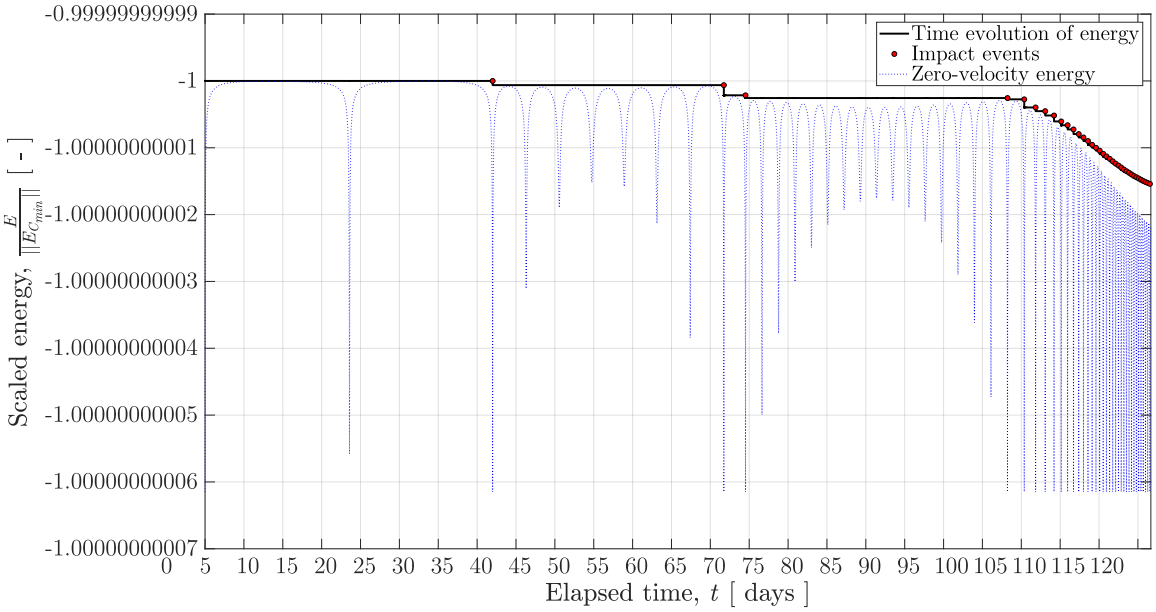

Fig. 13: Time history of the energy dissipation for a 10 cm particle ejected from $\theta = 0°$ with a curtain angle $\gamma = 20°$. Off nominal conditions: $\varepsilon_n = 0.84$, $\varepsilon_t = 1$, 4 months integration time

5.3 Eccentricity-ϕ phase space

To draw more significant conclusions or to predict the re-impact of particles for each specific case, full numerical propagation should be needed, which is time consuming and not particularly efficient [7]. For this reason, a semi-analytical approach is used to study the behaviour of dust dynamics perturbed by SRP and J_2, which is then compared to the numerical results. The widely used approach is to develop a method which focuses on orbital elements variation in time, rather than dealing with position and velocity vectors. In particular, Hamilton and Krivov [4] investigated the behaviour of circumplanetary dust in

where ϕ is the solar phase angle, Ω is right ascension of the ascending node of the particle orbit around the asteroid, i and ω are respectively the inclination and the longitude of pericentre, while λ_s is the solar longitude with respect to the Sun direction. As schematically shown in Fig. 14, ϕ represents the angle between the Sun-asteroid line and the direction of the orbit pericentre.

Due to the highly perturbed environment, orbits can pass from prograde ($0° \leq i < 90°$) to retrograde ($90° \leq i \leq 180°$) within few revolutions around the asteroid. Then, the inclination should be

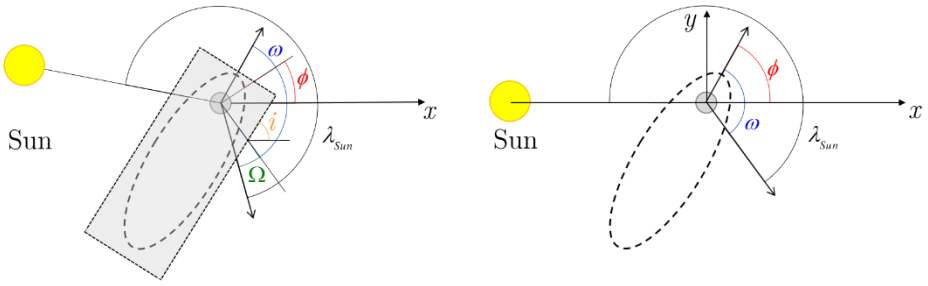

Fig. 14: Definition of the solar phase angle ϕ in the 3D case (left) and planar case (right)

taken into account even for the planar case, so that Eq. (21) turns into

$$\phi = \pm\omega - \lambda_s + \pi \tag{22}$$

where the sign of ω depends on the inclination.

The analytical orbit-averaged equations of motion written in the semicanonical form are [4], [5]:

$$\begin{cases} \dfrac{de}{d\lambda_s} = \dfrac{\sqrt{1-e^2}}{e}\dfrac{dH}{d\phi} \\ \dfrac{d\phi}{d\lambda_s} = -\dfrac{\sqrt{1-e^2}}{e}\dfrac{dH}{de} \end{cases} \tag{23}$$

where e is the orbits eccentricity, while the Hamiltonian H is given by

$$H = \sqrt{1-e^2} + \frac{1}{2}Ae^2\left[1+5\cos(2\phi)\right] + \\ -Ce\cos\phi + \frac{W}{3\left(1-e^2\right)^{3/2}} \tag{24}$$

which is an integral of motion, fixed by the initial conditions of the orbit. The above equations consider a planar problem, meaning that the orbit has zero inclination and the equatorial plane is assumed to be in the ecliptic one. Furthermore, the effect of the eclipses is also neglected and, as a consequence, the secular variation of semi-major axis and inclination is null [5]. Eq. (23) depends on the tidal parameter A, the solar radiation pressure parameter C and the oblateness parameter W, defined as

$$A = \frac{3}{4}\sqrt{\frac{n_s}{n}} \\ C = \frac{3}{2}a_{SRP}\frac{a^2}{\mu_a}\frac{n}{n_s} \\ W = \frac{3}{2}J_2\left(\frac{R}{a}\right)^2\frac{n}{n_s} \quad \text{, with} \quad \begin{cases} n = \sqrt{\dfrac{\mu_a}{a^3}} \\ n_s = \sqrt{\dfrac{\mu_s}{l^3}} \\ a_{SRP} = \beta\dfrac{\mu_s}{l^2} \end{cases} \tag{25}$$

where a is the orbit-averaged semi-major axis, a_{SRP} is the characteristic acceleration due to SRP defined in Eq. (2), μ_a and μ_s is the asteroid and Sun mass parameters, while n and n_s are the mean motion of the particle on its orbit and of the asteroid around the Sun, respectively.

While the initial argument of pericentre of the ejected particles can be arbitrarily chosen by selecting an ejection site/time [7], the initial eccentricity can be derived from the eccentricity vector definition, applied to the 2BP dynamics [16]

$$e_0 = \sqrt{1+\frac{h_0^2}{\mu_a^2}\left(v_0^2 - 2\frac{\mu_a}{r_a}\right)}, \quad h_0 = \left\|\mathbf{r}_0 \times \mathbf{v}_0\right\| \tag{26}$$

where h_0 is the specific initial angular momentum, defined by the initial position and velocity of ejection, while r_a is the asteroid mean radius.

As sketched in the previous figure, the x-y axes are now centred at the smaller primary location; indeed, the so-called eccentricity–ϕ phase space is naturally expressed in this reference frame. Then, to represent the previously integrated trajectories in this new framework, the origin of the reference frame should be shifted along the x-direction by a quantity $1-\mu$ to coincide with the asteroid. This changes the expression of the total potential of Eq. (11), which becomes

$$V = \frac{1}{2}\bar{n}^2\left(x^2+y^2\right) + \frac{1}{2}\bar{n}^2\left(1-\mu\right)^2 + \bar{n}^2\left(1-\mu\right)x + \\ + \frac{\left(1-\mu\right)\left(1-\beta\right)}{r_{sp}} + \frac{\mu}{r_{ap}}\left[1 - \frac{1}{2}J_2\left(\frac{\bar{r}}{r_{ap}}\right)^2\left(3\frac{z^2}{r_{ap}^2}-1\right)\right] \tag{27}$$

5.3.1 SRP-only effect

The eccentricity–ϕ phase space represented

in Fig. 15 contains the previously generated trajectories, ejected from the first and second quadrants ($0° \leq \theta \leq 180°$), when only SRP is considered. The dotted black line refers to the critical eccentricity e_{cr}, computed as [5], [7]

$$e_{cr} = 1 - \frac{r_a}{a_0} \tag{28}$$

where a_0 is the initial semi-major axis, generally dependent on both the particle size (hence on β) and the ejection site θ. The critical eccentricity is the value for which the orbit pericentre is on the asteroid surface (or below), causing a re-impact. As the variation of a over one revolution is zero, and the ejection/re-impact takes place close to the pericentre, this approximation is accurate enough [7].

The apocentres and pericentres of the numerically integrated trajectories have been indicated with $\times$ and $\bigcirc$ markers, respectively. Any pericentre taking place above the critical eccentricity line implies a re-impact; indeed, whenever the eccentricity is lower than the critical value by the first pericentre, the particle manages to perform multiple revolutions.

The red line refers to a particular multi-revolution trajectory ($\theta = 85°$): the osculating ellipse has an initial high eccentricity ($e \approx 0.92$), which starts to decrease and to circularise due to the SRP effect, down to a value of 0.1 approximately. Then, it progressively increases its eccentricity up to when it re-impacts the asteroid surface with a value of about 0.82. The evolution of apocenters can be followed in both Fig. 15 and Fig. 17: from the first apocenter right after the ejection (A), to apocenters (B) and (C) which are associated to the orbit's circularisation and finally the last one before impact (D).

The gray lines refer to the isolines of constant Hamiltonian that the orbit-averaged elements should follow in the analytical approach, with $W = 0$ in Eq. (24) (no J_2). When compared to the results obtained by Colombo et al. [5], no equilibrium points are found in the phase space due to the high SRP perturbation, as reported also by Garcia et al. [7]. Indeed, no stable orbit can be found around the asteroid, since the eccentricity starts eventually to increase causing a re-impact or, for high area-to-mass ratios (*i.e.* very small particles), a hyperbolic escape. The reason why the numerical behaviour slightly differs from the analytical approximation is due to two main reasons: first, the Hamiltonian approach is based on orbit-averaged values. This is an accurate assumption for circumplanetary dust dynamics, where a does not change over one revolution and the eccentricity changes slowly. However, for particles around small

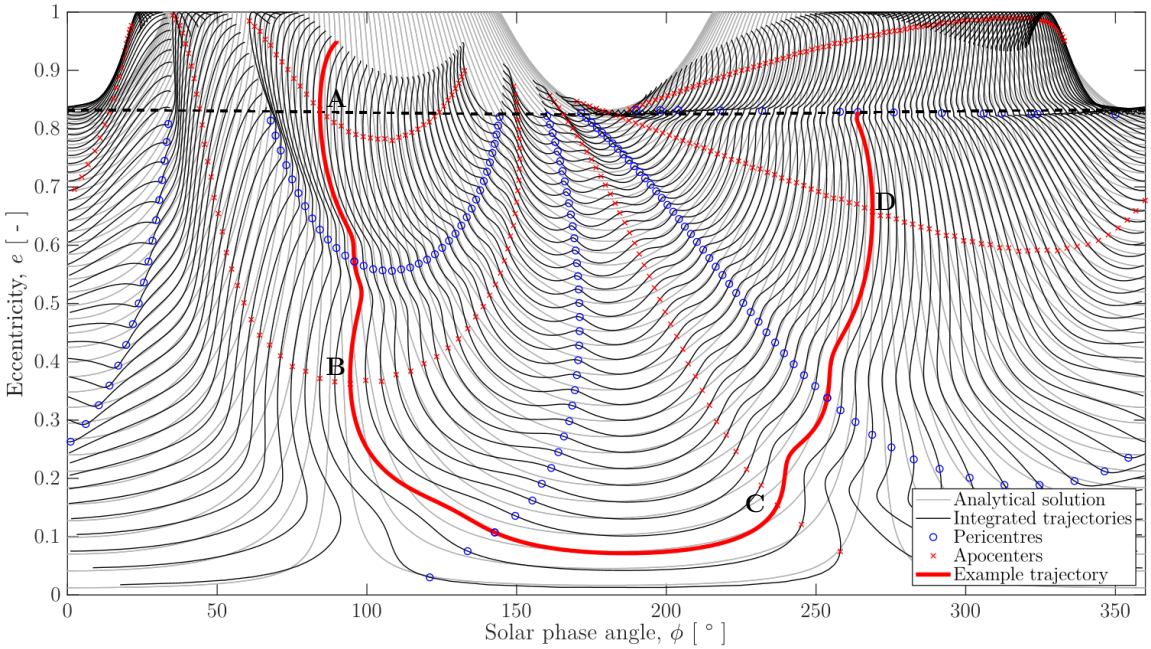

Fig. 15: Analytical (grey) and numerical (black) trajectories for 1st and 2nd quadrants ejection sites for SRP-only perturbed trajectories, with $C = C_2$ and $r_p = 1$ cm.

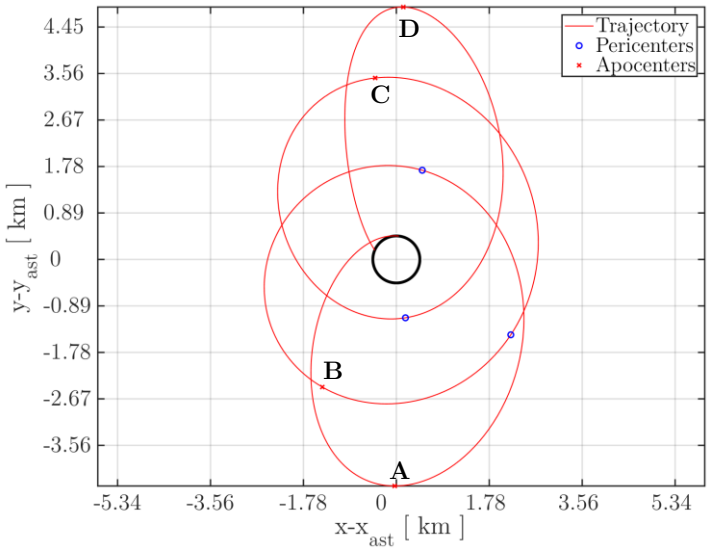

Fig. 17: Example trajectory showing the evolution of the osculating ellipse

bodies, the semi-major axis and eccentricity and eccentricity variations are much larger [7]. Secondly, the gravitational perturbation of the Sun plays an important role in shaping the orbits within the CR3BP, while in the analytical solution only the first tidal term A has been considered.

5.3.2 *SRP+J_2* effect

When the perturbation due to the asteroid oblateness is added, both in the numerical propagated trajectories and in the Hamiltonian analytical solution ($W \neq 0$), the regions of the stable equilibrium points ($\phi = 0°$ and $\phi = 180°$) start appearing, as visible in Fig. 16. As pointed out by Colombo et al. [5], the existence of stationary points is highly dependent on the semi-major axis and the lightness parameter of the orbiting object, which in turns determine the SRP and oblateness parameters C and W. At low semi-major axes, only the equilibrium point at $\phi = 0°$ exists, while

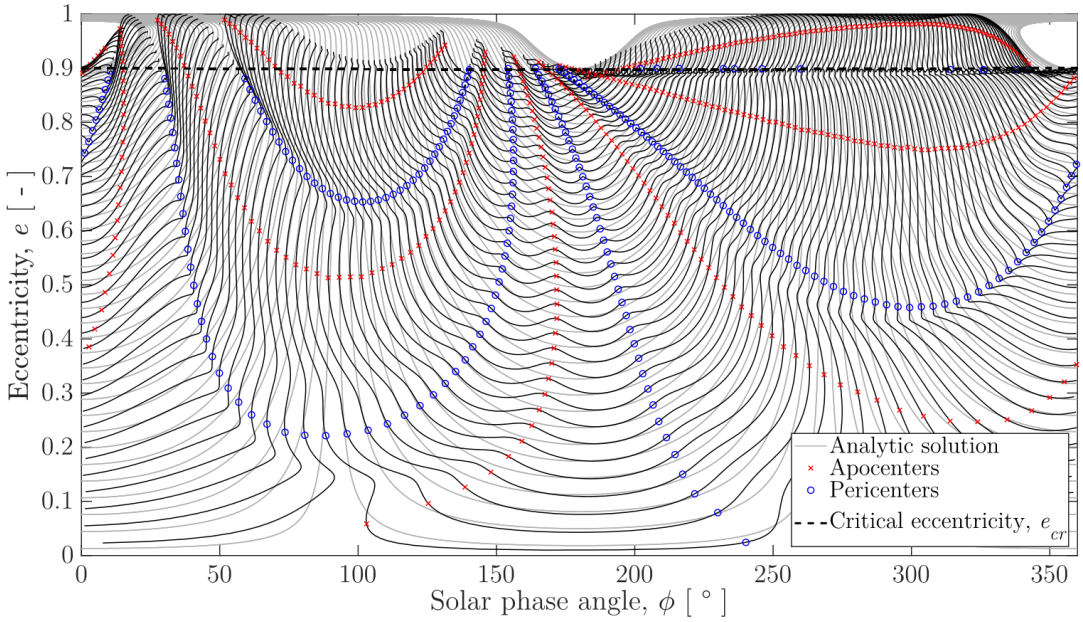

Fig. 16: Analytical (grey) and numerical (black) trajectories for 1st and 2nd quadrants ejection sites for SRP+J_2 perturbed trajectories, with $C = C_2$ and $r_p = 1$ cm

for increasing values of a another equilibrium point appears at $\phi = 180°$. However, these regions are above the critical eccentricity, meaning that they are unreachable prior the re-impact of ejecta on the asteroid surface.

5.4 On orbit collection

To predict the time evolution of apocenters and pericentres analytically, Garcia et al. [7] proposed, based on the work of Oyama et al. [17], to discard the tidal parameter A from the Hamiltonian, which in his model did not contained the term associated to the asteroid oblateness. In this thesis, instead, both the third body effect and the asteroid oblateness are retained in the equations of motion. From the correspondent generated trajectories, it is possible to extract the apocenters time evolution, as function of the particle size (or density), as shown in Fig. 18, in which a trend can be clearly appreciated.

The first apocenter occurrences (+ marker) are shifted in time, depending on the particle dimensions: larger particles require more time to reach the first apocenter with respect to small ones, which are more affected by the SRP perturbation. For mm-sized particles, the initial highly elliptical orbit circularises very quickly: for 1 mm ejecta, the first apocenter occurrence can be associated to eccentricities of almost 0.3. As the particle size increases, the first apocenter is reached more slowly, and it is located on high-eccentricity orbits. The second apocenter (○ marker) is associated to more circular orbits, regardless the particle size, while the third apocenter occurrences (• marker) are related to both high and low eccentricities, depending on the particle size. In particular, 1 mm particles could impact before the third apocenter occurs. Fig. 19, in which the discretisation in terms of lightness parameter is finer, confirms the trend of the first apocenter occurrences, showing that big particles reach the collection point slower than small ones.

6.Conclusions

The aim of this paper is to understand the dynamics of ejecta around a small body, in an environment perturbed by SRP and asteroid's oblateness. The complexity added by the bouncing mechanism on the asteroid surface is also addressed, with particular attention on how the energy of the system is damped through the non-elastic collisions. Indeed, the dissipation is proven to be highly dependent on the normal coefficient of restitution of the asteroid, as well as on the impact angle relative to the surface.

The eccentricity-ϕ phase space plots show

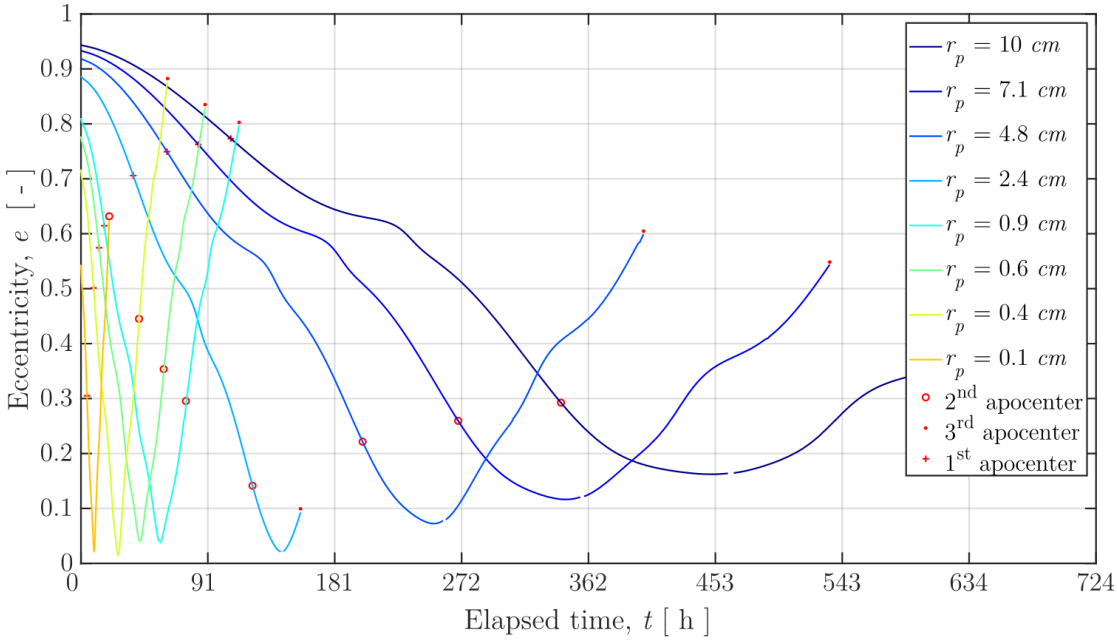

Fig. 18: Apocenters time evolution as function of the eccentricity

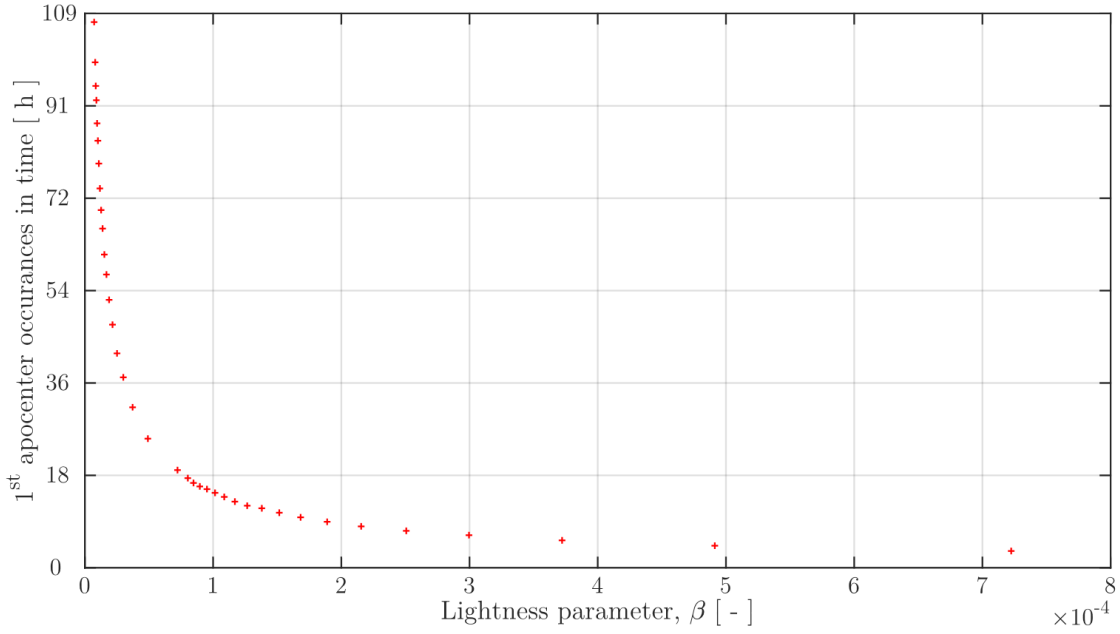

Fig. 19: First apocenters occurrences in time as function of the lightness parameter

good accordance between the numerical and analytical results. A series of guidelines can be deduced from these figures: the evolution of the osculating ellipse allows to identify for which ejection sites the trajectory is more likely to circularize in time. The apocenters and pericentres occurrences can be observed as well: it is possible to passively separate and collect particles in time, based on their size, by predicting the apocenters evolution in time.

The apocenter is the most suited collection point for an orbiting (or hoovering) spacecraft, since the associated velocity of the particles is the lowest one. Furthermore, being the most distant points from the asteroid surface, apocenters are the safest location to plan a collection manoeuvre, since it would allow to perform an emergency escape in a region which is not allowed to particles to naturally move into.

Acknoledgements

This work was supported by the European Research Council (ERC) under the European Union's Horizon 2020 research and innovation programme as part of project COMPASS (Control for Orbit Manoeuvring through Perturbations for Application to Space Systems), grant agreement 679086.

References

[1] B. E. Clark, B. Hapke, C. Pieters, and D. Britt, "Asteroid Space Weathering and Regolith Evolution," *Asteroids III*, 2002.

[2] D. V. Pinto, J. Heiligers, and S. Soldini, "Temporary Capture of Asteroid Ejecta into Periodic Orbits: Application to JAXA's Hayabusa2 Impact Event."

[3] A. V. Krivov, L. L. Sokolov, and V. V. Dikarev, "Dynamics of Mars-orbiting dust: effects of light pressure and planetary oblateness," pp. 313–339, 1996.

[4] D. P. Hamilton and A. V. Krivov, "Circumplanetary dust dynamics: Effects of solar gravity, radiation pressure, planetary oblateness, and electromagnetism," *Icarus*, vol. 123, no. 2, pp. 503–523, 1996.

[5] C. Colombo, C. Lücking, and C. R. McLnnes, "Orbital dynamics of high area-to-mass ratio spacecraft with J2 and solar radiation pressure for novel Earth observation and communication services," *Acta Astronaut.*, vol. 81, no. 1, pp. 137–150, 2012.

[6] R. P. Russell, D. Lantukh, and S. B. Broschart, "Heliotropic Orbits with Zonal Gravity and Shadow Perturbations: Application at Bennu," *J. Guid. Control. Dyn.*, vol. 39, no. 9, pp. 1925–1933, 2016.

[7] D. García Yárnoz, J. P. Sánchez Cuartielles, and C. R. McInnes, "Passive sorting of asteroid material using solar radiation pressure," *Adv. Astronaut. Sci.*, vol. 148, no. July, pp. 969–988, 2013.

[8] C. R. McInnes, "Solar radiation pressure," *Sol. Sail.*, pp. 32–55, 1999.

[9] J. D. M. James, "Celestial Mechanics Notes Set 4 : The Circular Restricted Three Body Problem," pp. 1–65, 2006.

[10] E. I. Abouelmagd and J. L. G. Guirao, "On the perturbed restricted three-body problem," *Appl. Math. Nonlinear Sci.*, vol. 1, no. 1, pp. 123–144, 2016.

[11] W. Boyce, "Comment on a formula for the gravitational harmonic coefficients of a triaxial ellipsoid," pp. 107–110, 1997.

[12] S. Soldini and Y. Tsuda, "Assessing the Hazard Posed by Ryugu Ejecta Dynamics on Hayabusa2 Spacecraft," *26th Int. Symp. Sp. Flight Dyn.*, 2017.

[13] Y. Yu, *Orbital Dynamics in the Gravitational Field of Small Bodies*. Springer Nature, 2016.

[14] S. Van Wal, Y. Tsuda, K. Yoshikawa, A. Miura, S. Tanaka, and D. Scheeres, "Prearrival Deployment Analysis of Rovers on Hayabusa2," vol. 55, no. 4, 2018.

[15] S. Tardivel, P. Michel, and D. J. Scheeres, "Deployment of a lander on the binary asteroid (175706) 1996 FG3 , potential target of the european MarcoPolo-R sample return mission," *Acta Astronaut.*, vol. 89, pp. 60–70, 2013.

[16] H. D. Curtis *et al.*, *Orbital Mechanics for Engineering Students Third Edition Butterworth-Heinemann is an imprint of Elsevier*. 2014.

[17] T. Oyama, H. Yamakawa, and Y. Omura, "Orbital Dynamics of Solar Sails for Geomagnetic Tail Exploration," *J. Spacecr. Rockets*, 2008.